Smart rotors

Dynamic-stall load control by means of an actuated flap

Raiola, Marco; Discetti, Stefano; Ianiro, Andrea; Samara, Farid; Avallone, Francesco; Ragni, Daniele

DOI
10.2514/1.J056342

Publication date
2018

Document Version
Final published version

Published in
AIAA Journal: devoted to aerospace research and development

Citation (APA)
Raiola, M., Discetti, S., Ianiro, A., Samara, F., Avallone, F., & Ragni, D. (2018). Smart rotors: Dynamic-stall load control by means of an actuated flap. *AIAA Journal: devoted to aerospace research and development*, *56*(4), 1388-1401. https://doi.org/10.2514/1.J056342

AIAA JOURNAL
Vol. 56, No. 4, April 2018

Smart Rotors: Dynamic-Stall Load Control by Means of an Actuated Flap

Marco Raiola,* Stefano Discetti,† and Andrea Ianiro‡
Charles III University of Madrid, 28911 Leganés, Spain
Farid Samara§
University of Waterloo, Waterloo, Ontario N2L 3G1, Canada
and
Francesco Avallone¶ and Daniele Ragni**
Delft University of Technology, 2629HS Delft, The Netherlands

DOI: 10.2514/1.J056342

This study focuses on an active strategy for unsteady-load control by means of a trailing-edge flap. Experiments on a 2D pitching and heaving NACA 0018 airfoil with an actuated trailing-edge flap are performed at a reduced frequency $k = 0.1$ in a free-stream flow with $Re = 1.3 \times 10^5$. The model is equipped with 24 differential pressure transducers to provide with the time-resolved distribution of the pressure difference between pressure and suction sides. Results show that an actuated flap significantly decreases the magnitude of unsteady loads. A reduced order model of the flap effect on the loads is proposed. The loads are estimated by adding the contribution of the clean wing with the flap one. This model can be applied to unsteady loads for both attached flow and dynamic stall conditions, constituting an effective control strategy for dynamic loads, if the airfoil transition location is properly controlled.

Nomenclature

$\mathcal{AR}$	=	wing aspect ratio
C_l	=	airfoil lift coefficient
$C_{l\alpha}$	=	airfoil lift curve slope
C_{l0}	=	airfoil zero incidence lift coefficient
C_m	=	airfoil pitching moment coefficient
C_{m0}	=	airfoil zero incidence pitching moment coefficient
C_p	=	pressure coefficient
c	=	airfoil chord, m
e	=	turbulent kinetic energy, $\mathrm{m}^2 \cdot \mathrm{s}^{-2}$
f	=	motion frequency, s^{-1}
h	=	heaving position, m
h_0	=	heaving amplitude, m
k	=	reduced frequency
p	=	static pressure, Pa
Re	=	Reynolds number
St	=	Strouhal number
V_∞	=	free-stream velocity, $\mathrm{m} \cdot \mathrm{s}^{-1}$
α	=	geometric angle of attack of the airfoil, deg
α_F	=	flap deflection angle, deg
α_m	=	mean geometric angle of attack of the airfoil, deg
α_0	=	pitching amplitude, deg
$\alpha_{0,F}$	=	flap deflection amplitude, deg
ϕ	=	phase shift between flap motion and heaving motion, deg
ψ	=	phase shift between pitching and heaving, deg
ρ_∞	=	freestream air density, $\mathrm{kg} \cdot \mathrm{m}^{-3}$
τ	=	motion period, s

Presented as Paper 2016-4242 at the 8th AIAA Flow Control Conference, Washington, D.C., 13–16 June 2016; received 19 May 2017; revision received 15 November 2017; accepted for publication 26 November 2017; published online 28 December 2017.

*Ph.D. Candidate, Aerospace Engineering Group; mraiola@ing.uc3m.es.
†Visiting Professor, Aerospace Engineering Group; sdiscett@ing.uc3m.es.
‡Visiting Professor, Aerospace Engineering Group; aianiro@ing.uc3m.es. Senior Member AIAA.
§Ph.D. Candidate, Wind Energy Group; farid.samara@uwaterloo.ca.
¶Assistant Professor, Aerodynamics, Wind Energy, Flight Performance and Propulsion (AWEP) Department; F.Avallone@tudelft.nl. Member AIAA.
**Assistant Professor, Aerodynamics, Wind Energy, Flight Performance and Propulsion (AWEP) Department; D.Ragni@tudelft.nl. Member AIAA (Corresponding Author).

I. Introduction

In THE last decade, the increasing need of wind energy production has led to manufacturing of large wind turbines. Relevant examples are the Siemens SWT-7.0-154 (featuring a 154 m rotor diameter) and the LM 88.4 P (with a 170 m rotor diameter). As a consequence, structural integrity and stiffness have become of paramount importance, thus affecting the final cost of energy. A possible strategy to reduce material and structural costs is to mitigate fatigue loads induced by unsteady flow conditions. One technological solution is the *Smart Rotor*, in which the dynamic loads are controlled by means of an active modification of the blades shape. The control is based on the feedback provided by sensors embedded in the turbine design [1].

Wind turbines are subjected to unsteady flow conditions depending on the wind farm arrangement and atmospheric turbulence. Considering the case of a heaving airfoil, unsteady effects are quantified by means of the reduced frequency $k = \pi c f / V_\infty$ and the Strouhal number $St = 2h_0 f / V_\infty$, where c is the airfoil chord, h_0 is the heaving semi-amplitude, f is the frequency, and V_∞ is the free-stream velocity. Corke and Thomas [2] set $k < 0.05$ as a reference rule to neglect unsteady effects.

For higher reduced frequencies, the blade may be subjected to dynamic stall, a regime characterized by nonlinear variations of the aerodynamic loads with the angle of attack [3]. The dynamic stall is an unsteady phenomenon that affects wings in a periodical motion [2,4]. Under these conditions, the aerodynamic stall is delayed to an angle of attack larger than the static one, thus causing aerodynamic loads higher than expected [4]. This typically leads to the generation of additional periodic forces and moments [5]. The dynamic stall is usually beneficial for birds and insects, because it allows to increase the maximum lift-to-mass ratio [6]. On the other hand, in helicopters [7–9] and wind turbines [3,10] this phenomenon entails large vibrations of their blades.

The dynamic stall is characterized by the formation of a leading edge vortex (LEV) [11] on the suction side of the airfoil, which prevents the complete separation of the boundary layer at post-stall angles of attack. The LEV is a flow structure that typically grows with increasing angle of attack [12], being fed by the vorticity developed in the boundary layer at the leading edge. During its growth the LEV brings an additional suction on the leading edge until its detachment.

The detachment of the LEV from the surface is characterized by an abrupt flow separation and thus by a severe lift loss. The LEV is responsible for the enhancement of aerodynamic forces on the wing, because it usually entails a strong low-pressure peak close to the nose of the airfoil. Because the variation of lift caused by LEV can be seen as a localized change in circulation [13], the control of the latter is fundamental to reduce the fluctuations of the aerodynamic loads in devices operating under unsteady conditions. Several studies attempted to isolate the dominant parameters to which dynamic stall is most sensitive. Baik et al. [12] pointed out that the LEV generation and growth are mostly influenced by the wing kinematics. Recent attempts to control the vortex dynamics by means of modifications of the wing kinematics revealed to be promising. For instance, quick pitch maneuvers [14] have been shown to have the potential of reducing the negative effects of the dynamic stall (such as increased drag and pitching moment) without affecting the lift augmentation associated with the LEV. However, the vortex control by means of the wing motion does not appear suitable for wind turbine applications, due to the significant increase of weight and complexity that it requires. A different approach consists of the active control of the boundary layer at the leading edge, for example, leading-edge blowing [15–17], leading-edge plasma actuation [5,18,19], vortex generators [20–22], and synthetic jets [23–25]. Alternatively, modification of the wing shape can be used to attenuate the dynamic stall effects. A very promising technology is the trailing edge flap (TEF) [26–30]. The main advantage of a TEF (and of trailing edge shape-morphing systems, in general) is the higher control authority per unit of added mass on the aerodynamic loads with respect to leading edge control systems (see, e.g., [1]). Gerontakos and Lee [29] investigated the effect of TEF deflection on the LEV formation and detachment. At a given positive angle of attack of the airfoil (see Fig. 1 for angle orientation), an upward flap deflection leads to a thinner and weaker LEV with respect to the clean wing; on the other side, a downward flap deflection results in a thicker and stronger LEV. The overall effect determined by the TEF movement is rather similar to a change of location of the stagnation point. For upward flap deflections the circulation reduces and the stagnation point moves toward the suction side. With lower centrifugal acceleration, the thickness of the LEV reduces, whereas the vortex increases in length. Although the TEF is not capable to control the formation and the detachment of the LEV, the changes in circulation produced by the LEV can affect the final loads on the wing, if compared with the zero-flap-angle condition.

The promising capabilities of the TEF make it a potential candidate for active shape-morphing *Smart Rotor* blades. On a real rotor blade, several flaps might be installed along the span in order to account for the inherent three-dimensionality of the flow on the blade. Typically, applications of flaps close to the tip, where the velocity reaches the highest magnitude, shall suffice for load control (see [31]) due to the high control authority of these devices. A similar technology has been already implemented in several smart rotor designs, both related with wind energy generation (see, e.g., [32]) or with helicopter rotors (see, e.g., [33,34]). However, while in steady cases linear models of actuations are typically sufficient for an effective control of the maximum load intensity [35], the extension to dynamic cases is not straightforward. The present work is devoted to bridge this gap and verify the limits of a linear modeling of the loads induced by the TEF for *Smart Rotor* applications. An experimental campaign is carried out on a 2D wing moving in a steady flow at $Re = 1.3 \times 10^5$ and reduced frequency $k = 0.1$. Time-resolved surface pressure data are recorded to monitor the unsteady loads and the effects of the TEF actuation. The variation of the loads induced by the flap is studied for both steady and dynamic conditions and compared with the configuration with zero flap deflection. Finally, a linear model for TEF actuation performances is proposed and validated.

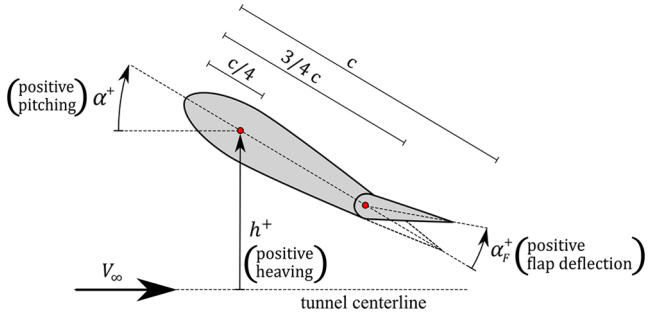

Fig. 1 A sketch of the flapping wing degrees of freedom.

II. Experimental Setup

The experiments are carried out in the Open Jet Facility (OJF) at TU Delft. The OJF is an open-jet wind tunnel with nozzle dimensions of 285×285 cm^2. The turbulence intensity is approximately 0.5% and 2% at a distance of 1 and 6 m from the nozzle exit [36], respectively. The flow temperature is kept constant at 20°C through a heat exchanger. The wind tunnel is operated at a free-stream velocity of 5 m/s, entailing a chord-based Reynolds number of 1.3×10^5 for the tested model. The choice of the free-stream velocity (and thus of the Reynolds number) is based upon a compromise between high-enough reduced frequencies to introduce unsteady aerodynamic effects and limited flapping frequencies of the wing, in order to avoid structural vibrations of the model. Because the chosen Reynolds-number regime is characterized by laminar-turbulent transition effects, in the following these effects are isolated by considering both a free-transition case and a forced-transition one.

The tested wing model is obtained from extrusion of a NACA 0018 profile, with chord $c = 400$ mm and aspect ratio $\mathcal{AR} = 4$. To reduce the wing tip vortices, circular side plates of 800 mm diameter are installed on both wing tips, as shown in Fig. 2. The wing trailing edge is modified to house a plain flap with hinge point at $3/4c$ from the leading edge. The flap chord has been chosen to maximize the control authority and effectively reduce the load peaks arising during dynamic stall. For instance, configurations with similar flap size have been successfully employed for helicopter rotors in [33]. Moreover, having a relatively large flap chord is also beneficial for experimental purposes because it allows embedding pressure sensors within the flap. It has to be remarked that the flap chord length represents an important design parameter of the control system and it must be

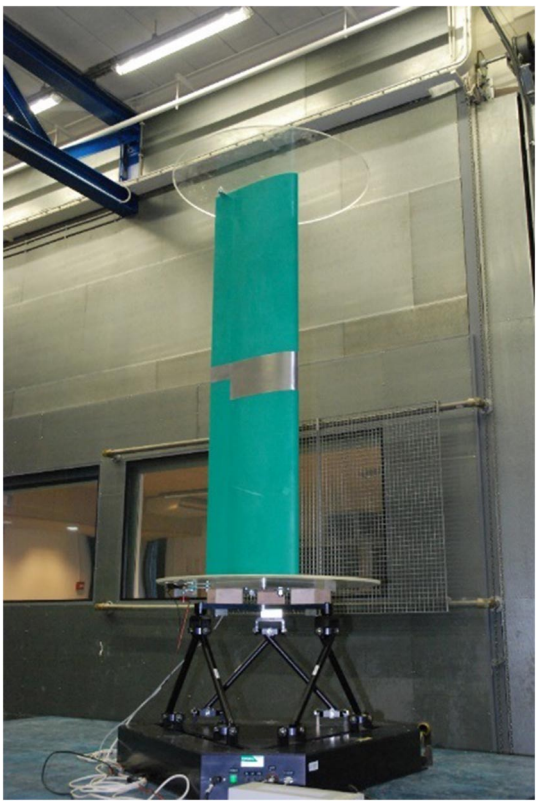

Fig. 2 The wing model on the 6-DOF platform.

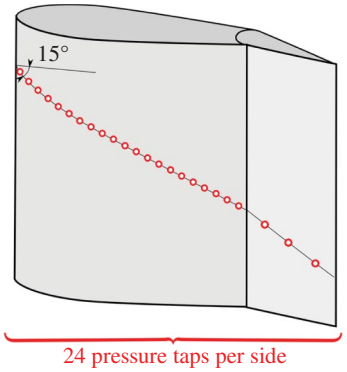

Fig. 3 Sketch of the middle section equipped with the pressure taps.

chosen according to a compromise between load control authority and aerodynamic efficiency of the blade section. However, an optimization of this parameter is out of the scope of the present study. The deflection of the flap is provided by one high-voltage Horizon JR DS8711HV servomotor. The maximum flap deflection is $\alpha_{F\,\max} = \pm 10°$ with respect to the clean wing chord.

The wing is equipped with 24 Honeywell HSCSRRN1.6MDSA5 differential pressure transducers (3 kHz max acquisition frequency, ±0.004 mbar accuracy), connected to 48 pressure taps (0.4 mm diameter). The transducers are embedded in the wing model, allowing for direct measurements of the local pressure difference between the upper and the lower sides of the wing. Pressure taps are placed along a 15° line with respect to the chord in order to reduce interference effects (Fig. 3). In the following, the measured pressure differences are presented normalized as $\Delta C_p = \Delta p/(1/2\rho_\infty V_\infty^2)$. For each case, the pressure is phase-averaged over 50 flapping periods. The uncertainty on the phase-averaged ΔC_p is estimated to be lower than 0.04, by following the estimation method by Moffat [37]. Differential pressure data are integrated along the chord to measure the aerodynamic forces: lift and pitching moment coefficients (the latter measured with respect to the $1/4c$ point, positive for pitching up moments). The force resulting from the pressure-difference integration is oriented in the normal-to-chord direction. The lift force has been calculated, with good approximation, as the projection of this force in the wind reference frame (given the geometric angle of attack), thus neglecting the parallel-to-chord force component, which could not be measured with the present setup. The parallel-to-chord force component is instead expected to play a significant role for the determination of the drag, which for this reason is not accessible with the present experimental setup. The uncertainty on the phase-averaged lift and pitching moment coefficients is estimated [37] to be lower than 0.01 and 0.005, respectively. Forces and pressure data are reported in the Results section as a function of the angle of attack after applying a correction for open test section wind tunnels [38].

Because of the low Reynolds number, both a stethoscope and pressure distribution measurements are used to detect the presence of a laminar-turbulent transition. Boundary-layer transition is forced by means of a zigzag strip (2 mm thick, 12 mm wide, with 60° angle) placed at $0.1c$. It is verified that, in static conditions, boundary-layer transition occurs immediately downstream of the turbulator for all the angles of attack investigated. Considering the sensitivity of the dynamic stall on the state of the boundary layer, the effects of the turbulator for both steady and dynamic conditions are discussed in the following.

Periodical flow conditions on the blade are reproduced by means of a sinusoidal flapping motion with Strouhal number $St = 0.006$ and reduced frequency $k = 0.1$. The movements featured both a pitching, that is, a variation of the geometrical angle of attack $\alpha(t)$, and a heaving motion, that is, a cross-stream displacement $h(t)$ of the airfoil. The heaving position is defined with respect to the position of the hinge point of the wing, placed at $1/4c$ from the leading edge, as sketched in Fig. 1. These motions are realized by means of a 6-degrees-of-freedom Quanser Hexapod robotic platform. The sinusoidal movement of the wing in heaving and pitching motions is set as

$$\begin{aligned} h(t) &= h_0 \sin(2\pi f t) \\ \alpha(t) &= \alpha_m + \alpha_0 \sin(2\pi f t - \pi/2) \end{aligned} \tag{1}$$

where f is the motion frequency, h_0 is the semi-amplitude of the heaving motion, α_m is the mean angle of attack, and α_0 is the semi-amplitude of the pitching motion. The system is operated with $f = 0.4$ Hz and $h_0 = 0.1c$. The phase delay between heaving and pitching motions is set to a quarter of the motion period τ in order to maximize the quasi-steady effective angle of attack. Two different wing kinematics are discussed in paragraphs III.C and III.D: a symmetric motion with $\alpha_m = 0°$ and $\alpha_0 = 10°$, referred to as dynamic test case A; an asymmetric motion with $\alpha_m = 9°$ and $\alpha_0 = 10°$, referred to as dynamic test case B. Test case A reaches angles of attack at the onset of the stall; test case B promotes the occurrence of deep stall.

The effective angle of attack is defined by combining the heaving and pitching motions, as

$$\begin{aligned} \alpha_{\text{eff}} &= \alpha - \tan^{-1}\left(\frac{1}{V_\infty}\frac{\partial h}{\partial t}\right) \\ &= \alpha_m + \alpha_0 \sin\left(2\pi f t - \frac{\pi}{2}\right) + \tan^{-1}\left(\pi St \sin\left(2\pi f t - \frac{\pi}{2}\right)\right) \end{aligned} \tag{2}$$

In Fig. 4 the difference between the geometric and the effective angle of attack is shown for both case A and case B. Because of the rather small Strouhal number, the difference between the geometric and the effective angle of attack is always smaller than 1°.

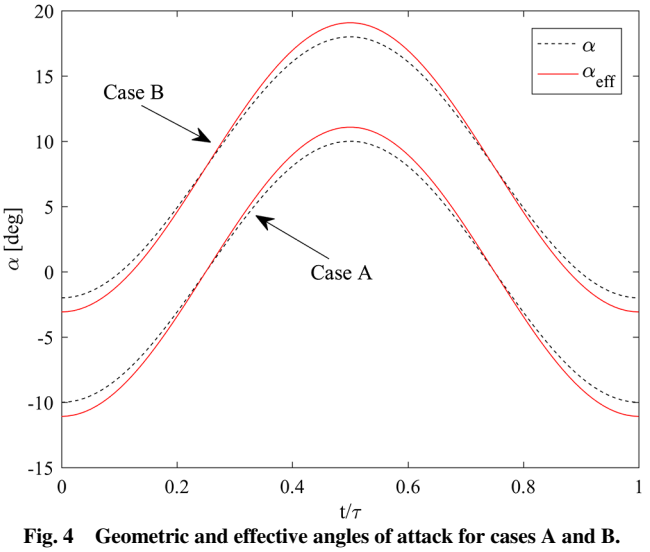

Fig. 4 Geometric and effective angles of attack for cases A and B.

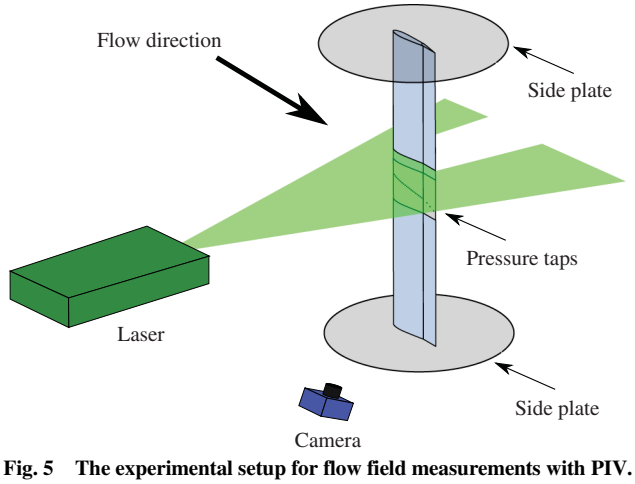

Fig. 5 The experimental setup for flow field measurements with PIV.

Table 1 PIV imaging and processing parameters

Parameters	Quantity	
Measurement field of view, *FOV*	401×267 mm^2	4872×3248 px^2
Interrogation window size, I_w	2×2 mm^2	24×24 px^2
Vector spacing, *S*	0.5 mm	6 px (75% ov.)
Digital resolution, *DR*	12.1 px/mm	
Magnification, *M*	0.09	

The flap is deflected imposing a sisoidal kinematic with the same frequency of the wing motion:

$$\alpha_F(t) = \alpha_{0,F} \sin(2\pi f t + \phi) \tag{3}$$

where $\alpha_{0,F}$ is the semi-amplitude of the deflection and ϕ is the phase shift with respect to the heaving motion. Note that, as shown in Fig. 1, an upward deflection corresponds to positive α_F, whereas a downward deflection to negative α_F.

Particle image velocimetry (PIV) measurements visualize the formation and the evolution of the LEV on the suction side of the wing. Figure 5 illustrates the PIV setup used to map the two-component velocity fields on one side of the wing at the midspan. The required illumination is provided by a Quantel Evergreen Nd:YAG laser system with 200 mJ/pulse energy at a frequency of 15 Hz (wavelength of 527 nm). The laser light is conveyed through laser optics to form a 2 mm laser sheet of about 405 mm width ($\sim 1c$). The laser head is positioned outside the open jet to reduce vibrations and flow interference. The laser sheet is located just above the pressure taps, approximately 0.37 c above the midline of the airfoil, and aligned with the chord.

A LaVision Imager Pro LX 16 Mpixels (4872×3248 px^2, 12 bits) with a pixel-pitch of 7.4 μm/px is used to image a field of view of 400×267 mm^2 at about 1 m distance, tilted of about 20 deg. The camera is equipped with a Nikon lens of 105 mm focal length set at aperture $f\# = 5.6$, thus resulting in a magnification of $M = 0.09$. A Scheimpflug adapter is used to correct for the camera angle. Seeding

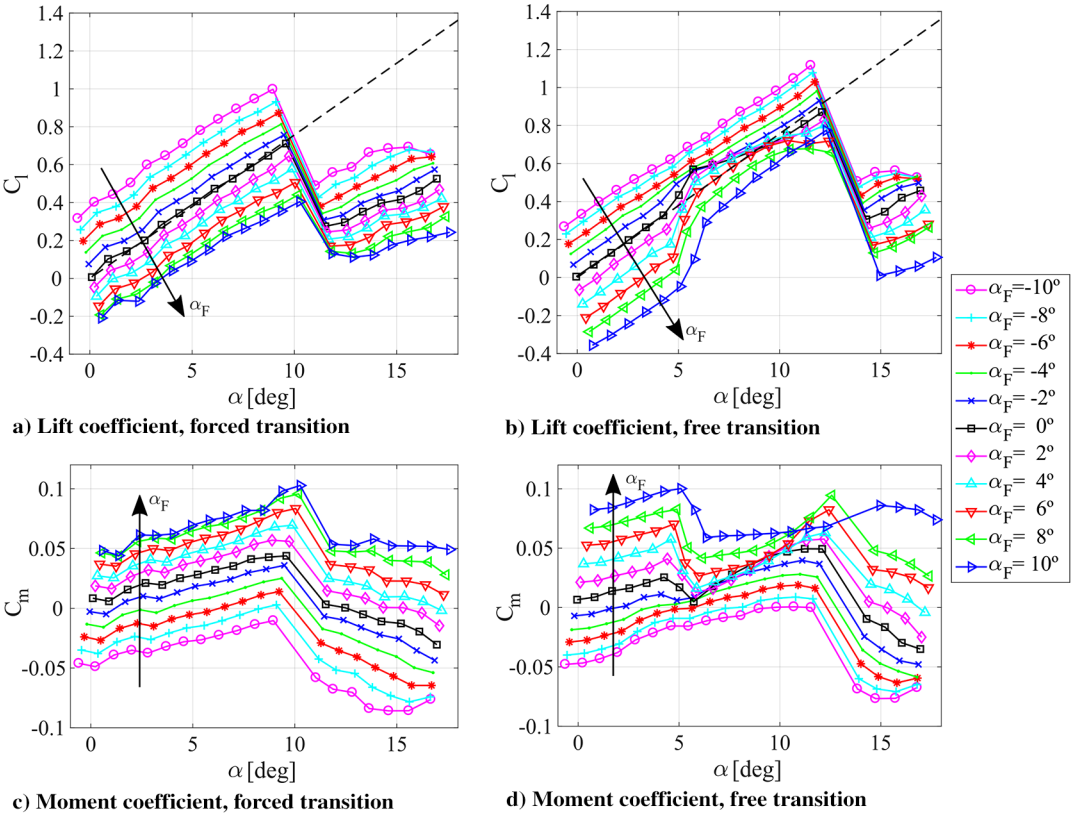

a) Lift coefficient, forced transition

b) Lift coefficient, free transition

c) Moment coefficient, forced transition

d) Moment coefficient, free transition

Fig. 6 Steady lift coefficient (C_l) and pitching moment coefficient (C_m) for forced transition and free transition.

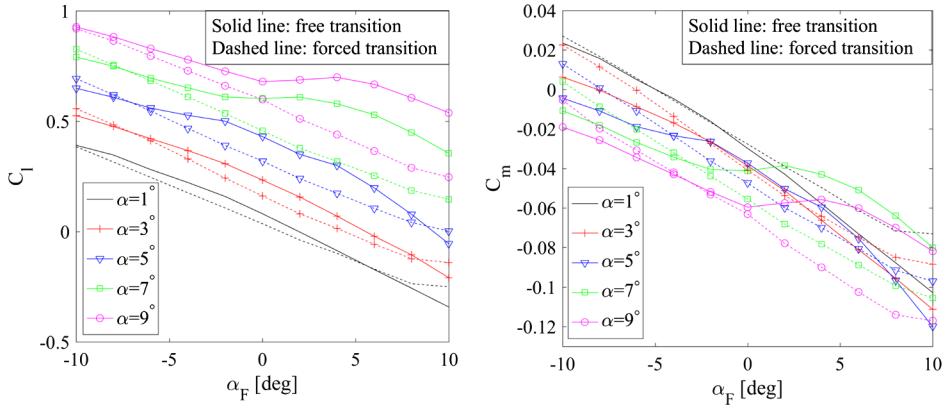

a) Lift coefficient

b) Pitching moment coefficient

Fig. 7 Effect of the flap on the loads in steady flow conditions.

particles are injected in the test section with a SAFEX smoke generator employing a SAFEX MIX, able to generate liquid droplets of less than 1 μm diameter.

A LaVision type 30 calibration plate was employed for the optical calibration. Particle images acquisition, calibration, and cross-correlation were carried out with *LaVision* DaVis 8.3.0. Phase-locked

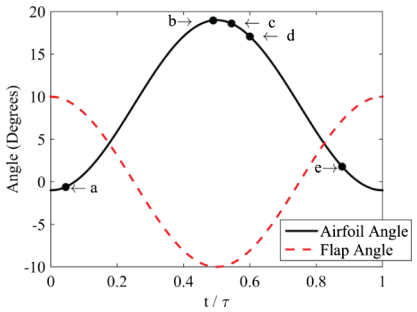

t/τ	Reference Point	Airfoil Angle	Flap Angle
0.04	(a)	-0.6°	9.6°
0.49	(b)	19.0°	-10.0°
0.54	(c)	18.6°	-9.6°
0.6	(d)	17.1°	-8.1°
0.88	(e)	1.8°	7.2

Fig. 8 Geometric angle of attack of the airfoil and flap angle over time. The dots represent the selected PIV phase-averaged fields illustrated in Fig. 9.

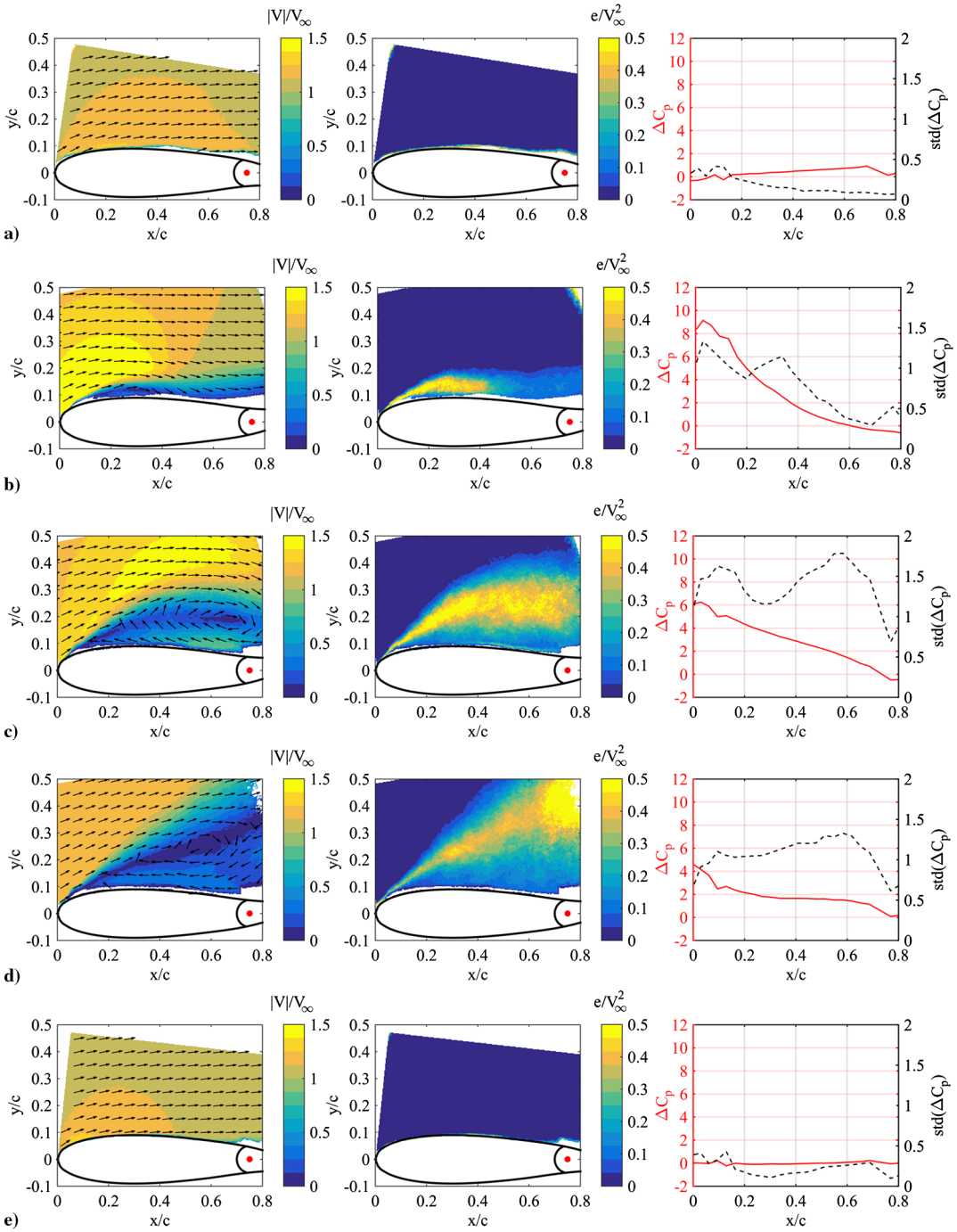

Fig. 9 Left) Velocity magnitude contour plots with superposed vector arrows. Center) Turbulent kinetic energy contour plots. Right) Phase-averaged mean and standard deviation of differential pressure coefficient. a)–e) Refers to selected time instants as in Fig. 8.

Table 2 Stall penetration angles for the cases studied

	Free transition	Fixed transition
Case A	$\alpha_{penetration} = 10° - 12° = -2°$	$\alpha_{penetration} = 10° - 9.5° = 0.5°$
Case B	$\alpha_{penetration} = 18° - 12° = 6°$	$\alpha_{penetration} = 18° - 9.5° = 8.5°$

PIV measurements are acquired using a trigger signal provided by a digital encoder installed in the hexapod. The flapping period is discretized in 20 phases with 100 pairs of particle images acquired per phase. Particle images are preprocessed to remove background noise and laser reflections [39]. After image preprocessing, a multipass algorithm is used for particle image correlation with a final window size of 24×24 px^2 and 75% overlap, corresponding to 2×2 mm^2 resolution and 0.5 mm vectors spacing. The PIV imaging and processing parameters are summarized in Table 1.

The main sources of uncertainty in the vector fields, with the present magnification and at the present Reynolds and Mach number, are cross-correlation uncertainty and the peak-locking. At the present magnification and aperture, the particle image size on the sensor is smaller than 1 pixel. Therefore, the focusing plane is slightly offset with respect to the laser plane (defocusing) to obtain an image of the particle of about 2–3 pixels, able to mitigate bias errors associated with peak-locking [40]. Mitigation of peak-locking errors is a posteriori verified by means of a decimal distribution histogram. The cross-correlation uncertainty on the particle displacement represents a random error that scales with the available number of samples per dataset, giving the most relevant contribution in the uncertainty of the velocity measurements. After calculation with the adapted magnification and separation time, the final uncertainty in the mean velocity field is assessed to be at 0.2% of the free-stream velocity, whereas the uncertainty in the turbulent statistics is assessed at 1% of the free-stream velocity.

III. Results

First, in Sec. III.A, measurements of the static loads acting on the wing are reported for different flap settings and for both free and forced boundary-layer transition. Subsequently, in Sec. III.B, the occurrence of deep dynamic stall (test case B) is investigated with PIV. The loads acting on the wing with flap angle set to zero are discussed in Sec. III.C for both test cases (A and B). The effect of the flap actuation on the loads are presented in Sec. III.D. Finally, in Sec. III.E, a linearized flap model is proposed. The model is tested on the actuated flap configurations to verify its suitability for dynamic stall conditions.

A. Steady Aerodynamic Loads

The static loads acting on the wing are measured for free and forced boundary-layer transition. The lift and moment coefficients are reported in Fig. 6 as a function of α and parametrized with α_F.

With forced transition, the lift coefficient C_l (Fig. 6a) is a linear function of α (up to the stall angle) with slope $C_{l\alpha} = 1.4\ \pi$/rad; the difference with respect to the conventional 2π/rad [35] slope is here ascribed to finite wing effects and it agrees with results from a panel method approach carried out with XFLR5 [41].

In the case of free transition, a first linear region for both C_l (Fig. 6b) and C_m (Fig. 6d) is measured for $\alpha_F \leq 4$. For higher angles of attack a sudden increase of C_l followed by a second linear region is measured. The slope of the lift coefficient $C_{l\alpha}$, in the first linear

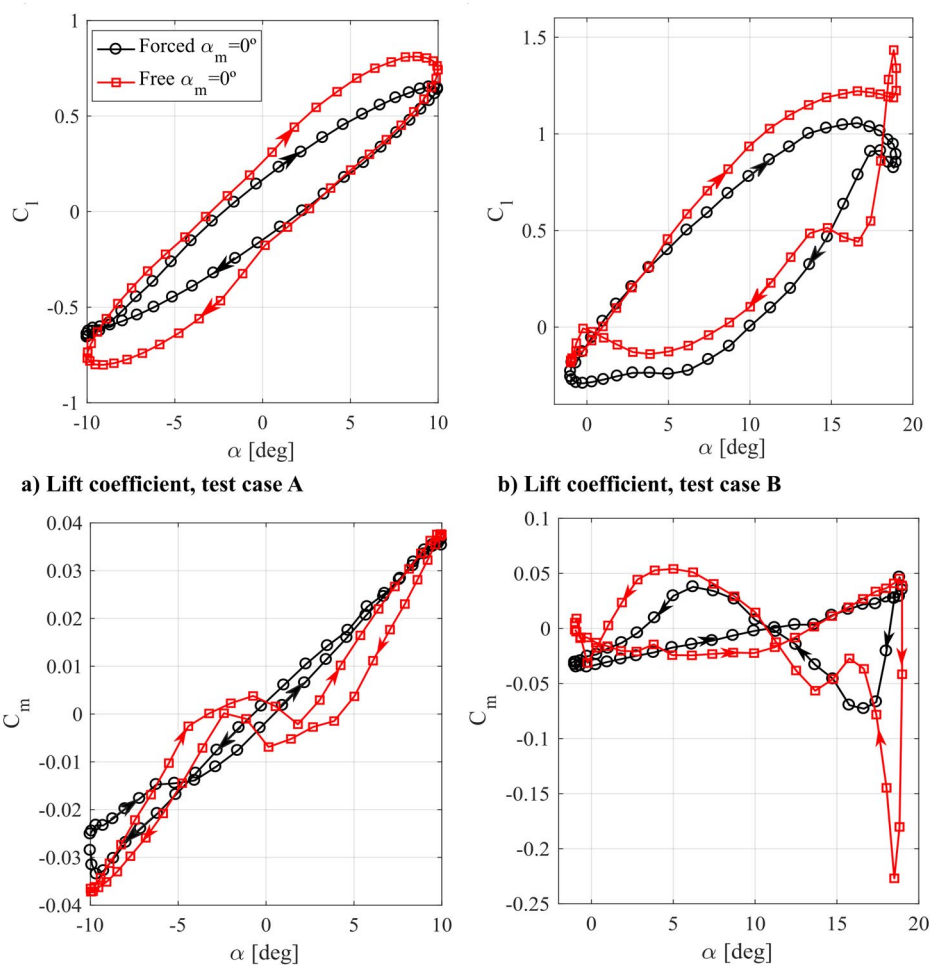

a) Lift coefficient, test case A

b) Lift coefficient, test case B

c) Pitching moment coefficient, test case A

d) Pitching moment coefficient, test case B

Fig. 10 Comparison of the lift coefficient (C_l) of the pitching moment coefficient (C_m) for forced and free transition.

region, is the same as the one measured for the forced transition case. In a similar study [42], this behavior of C_l was ascribed to the formation of a laminar bubble on the pressure side of the airfoil close to the trailing edge, which enhances the aerodynamic lift by locally changing the airfoil curvature. However, the increase in lift depends on α_F.

For large negative α_F, the reduction of the adverse pressure gradient due to the negative deflection might avoid the formation of the laminar bubble, thus resulting in a fully linear behavior.

The effects of the flap deflection in steady conditions are reported in Fig. 7 for several angles of attack of the wing and for both free and fixed transition conditions. For fixed transition cases both the lift and the aerodynamic moment coefficients are almost linear functions of the flap deflection with a slope that is not significantly influenced by the angle of attack. For free transition, instead, both the lift and the aerodynamic moment coefficients strongly depend on the angle of attack. Linearization of the load variations is acceptable only for small angles of attack and in general for negative flap deflections.

B. Flow Field Characterization

PIV measurements were carried out to visualize the dynamic stall and link the resulting flow features with the surface pressure measurements.

A sketch of the variation of the angle of attack during the cycle [Eq. (1)] for the test case B ($\alpha_m = 9°$) is reported in Fig. 8. The flap is actuated with phase shift $\phi = \pi/2$ [Eq. (3)] with respect to the wing motion. PIV phase-locked data are presented for the forced transition case in Fig. 9. The velocity fields are blanked to remove regions with low signal-to-noise ratio due to wall reflections. The left column of Fig. 9 presents contour plots of the velocity magnitude together with the vector fields (downsampled for clarity of visualization); the central column shows the in-plane turbulent kinetic energy $e = (1/2)(\overline{u'^2} + \overline{v'^2})$ (where u' and v' the fluctuating velocity component in the x and y directions, respectively); the right column reports the mean differential surface pressure coefficient ΔC_p (in red solid line) and its standard deviation (*std*, in dashed black line). The velocity data are normalized with respect to the free-stream velocity. The selected phases are indicated in Fig. 8 with black markers, and labeled with letters (a) to (e). The angle of attack and the flap angle for the selected phases are reported in the table in Fig. 8.

At $t/\tau = 0$ (Fig. 9a), the airfoil is at angle of attack approximately equal to zero. Results show that the flow remains attached due to the low pressure gradient. The measured ΔC_p is rather low, as a result of the quasi-symmetric distribution of C_p between the pressure and the suction sides of the wing. During the upstroke and in the first half of the downstroke, the flow remains attached even though the angle of attack increases beyond the static stall angle (Fig. 9b). At $t/\tau = 0.49$, the maximum angle of attack is reached ($\alpha = 19°$); at this stage the pressure difference between the pressure and suction sides reaches the absolute maximum intensity at the leading edge (Fig. 9b). The large value of ΔC_p is ascribed to the formation and growth of the LEV, attached to the airfoil in the range $0.1 < x/c < 0.4$. The turbulent kinetic energy shows a corresponding increase of the fluctuations intensity in the same region, suggesting the presence of a fluctuating behavior of the LEV between the different cycles. For $t/\tau = 0.54$, right after the reversal of the pitching movement, the LEV continues growing and progressively moves downstream of the airfoil (Fig. 9c). The presence of the LEV is characterized by large intensity of the turbulent kinetic energy and by a sudden increase of the std(ΔC_p). At $t/\tau = 0.60$ the LEV is fully detached from the airfoil (Fig. 9d), resulting in lower velocity magnitude and ΔC_p than at the pre-stall. The flow remains separated for the rest of the

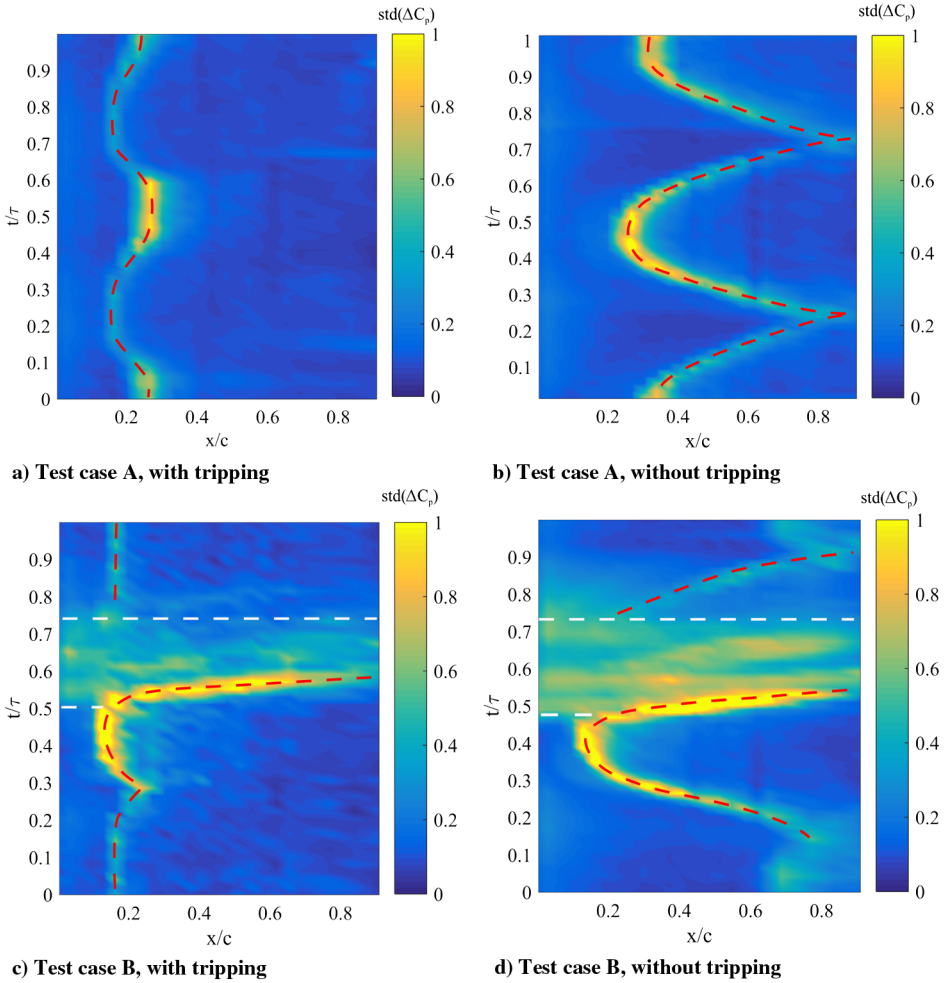

a) Test case A, with tripping **b) Test case A, without tripping**

c) Test case B, with tripping **d) Test case B, without tripping**

Fig. 11 Maps of the standard deviation of ΔC_p as a function of leading edge distance and of time.

downstroke cycle, then reattaching as the angle of attack decreases. Complete reattachment is observed at $t/\tau = 0.88$ (corresponding to $\alpha \approx 1.8°$).

C. Effect of Tripping in the Dynamic Configurations

The influence of the boundary-layer transition on the dynamic stall is investigated in this section. Both test cases A ($\alpha_m = 0°, \alpha_0 = 10°$) and B ($\alpha_m = 9°, \alpha_0 = 10°$) are discussed. The flap angle is $\alpha_F = 0°$, that is, clean wing configuration.

The expected flow behavior of the different cases can be addressed by means of the stall penetration angle (see [2]), defined as $\alpha_{\text{penetration}} = \alpha_{\text{max,dyn}} - \alpha_{\text{stall,steady}}$, with $\alpha_{\text{max,dyn}}$ and $\alpha_{\text{stall,steady}}$ being, respectively, the maximum angle of attack reached during the dynamic motion and the stall angle of attack in steady flow conditions. The stall penetration angles are summarized in Table 2.

According to the values reported, for case A the flow over the airfoil is expected to be in no-stall/onset-of-stall conditions and for case B it is expected to be in deep-stall conditions.

Figure 10 reports the C_l and C_m curves against the geometric angle of attack for both the test cases in clean wing configuration. The arrows indicate the phase direction of the load loops. In both dynamic cases, the C_l curve (Figs. 10a and 10b) presents an hysteresis cycle. The maximum C_l is higher than the one achieved in the steady configuration due to the presence of the LEV on the suction side as discussed in the previous section. The maximum C_m (Figs. 10c and 10d) is measured at the half of the downstroke cycle, that is, when the angle of attack is maximum. This is to be ascribed to the suction effect of the LEV, which is responsible of the increased lift at the leading edge, thus generating a pitch-up moment. It can be argued that, during the first half of the downstroke, the LEV dynamic is independent on the transition onset. During the second part of the downstroke, in both cases a pitch-down moment is generated. It is ascribed to the detachment of the LEV, as observed in Fig. 9d. This effect is stronger for the free transition configuration. The results suggest that forcing transition allows reducing the unsteady loads variation during the cycle, particularly at high α (test case B).

Test case B shows that C_l (Fig. 10b) increases beyond the maximum C_l achieved for the static case, until $\alpha \approx 16°$. The stall is postponed to α larger than the steady stall one (Fig. 6). The maximum C_l is equal to 1.5 for the free transition configuration and to 1.0 when the boundary layer is tripped. The higher C_l experienced in free transition could be explained by the possible presence of a laminar separation bubble at the trailing edge of the airfoil pressure side, as previously observed for the same airfoil in steady conditions [42]. For the free transition configuration, the hysteresis curve shows a local peak at $\alpha \approx 14°$ ($t/\tau \approx 0.66$), whereas when transition is forced the local peak occurs much earlier ($\alpha \approx 18°$, $t/\tau \approx 0.43$). This phenomenon might be ascribed to a sudden flow reattachment during the upstroke, anticipated in case of forced boundary layer.

The effect of forced transition on dynamic stall is further investigated by discussing the surface pressure fluctuations. The fluctuations intensity is reported in Fig. 11 in terms of standard deviation of ΔC_p as a function of the phase and chord location. The maxima of std(ΔC_p) are determined by the onset of transition (highlighted in Fig. 11 with red dashed lines). In Fig. 11b (test case A and free transition) the local maximum of ΔC_p shifts downstream when decreasing the angle of attack and it oscillates in the range $0.3 < x/c < 1$ with a nearly sinusoidal pattern. The frequency of the

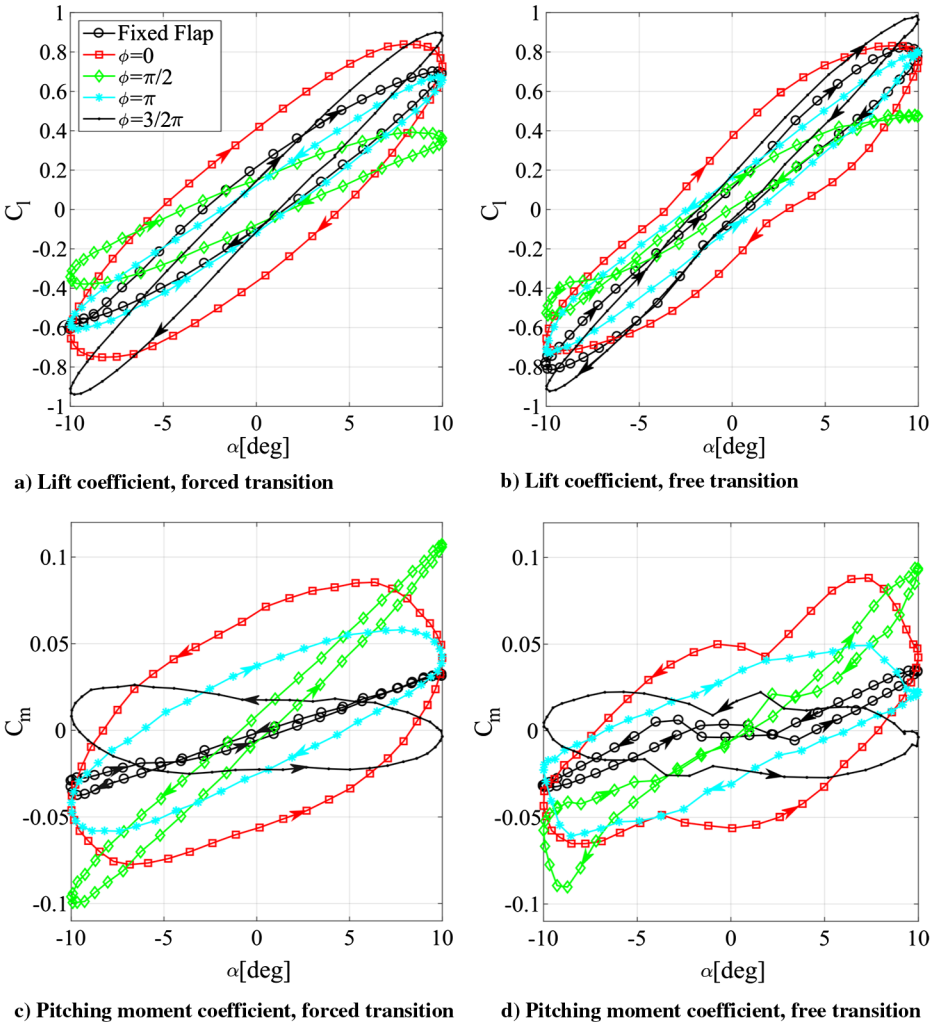

a) Lift coefficient, forced transition

b) Lift coefficient, free transition

c) Pitching moment coefficient, forced transition

d) Pitching moment coefficient, free transition

Fig. 12 Comparison of the lift and pitching moment coefficients for different flap actuation phases. Test case A: $\alpha_m = 0°$, $\alpha_{0,F} = 10°$.

fluctuation peak displacement is twice the frequency of the flapping motion. This is due to the occurrence of the transition on both sides of the airfoil (during one full cycle each side of the airfoil acts as suction or pressure surface for half of the cycle). Forcing of boundary-layer transition (Fig. 11a) locks the streamwise location of the maximum ΔC_p at $x/c \approx 0.2 \pm 0.05$. The position of the maximum ΔC_p confirms that the transition is imposed at the tripping location.

A different behavior is detected when increasing the mean angle of attack α_m (test case B, Figs. 11c and 11d), where for $0.5 < t/\tau < 0.8$ (corresponding to a progressively decreasing angle of attack), the intensity of the surface pressure fluctuations is higher along the entire chord (see the region delimited by white dashed lines in Figs. 11c and 11d). This effect can be associated to the formation and growth of the LEV on the suction side of the airfoil and to the consequent flow separation after the vortex detachment (as observed in the PIV measurements for $t/\tau \geq 0.5$). A comparison between the free (Fig. 11d) and the forced transition configurations (Fig. 11c) shows that these phenomena are not affected by the presence of the tripping in the part of the period with fully separated flow. The most relevant effect of the tripping is to reduce the intensity of std(ΔC_p). Similarly to the test case A, the presence of the tripping limits the displacement of the transition point for $t/\tau < 0.5$, that is, before the occurrence of the dynamic stall separation, and force it to the tripping location.

D. Effect of Flap Actuation

The effect of the flap actuation is reported in this section for different values of the phase delay ϕ with respect to heaving motion [Eq. (3)], for the dynamic test cases A and B. Pressure measurements are discussed with flap displacements as in Eq. (3) and ϕ ranging between 0 and 2π. The arrows in Figs. 12 and 13 indicate the phase direction of the load loops.

The effect of ϕ on the lift coefficient for test case A is plotted in Figs. 12a and 12b for forced and free transition, respectively. In both cases, the variation of C_l during the cycle is minimized for $\phi = \pi/2$, that is, when the flap is in phase with respect to the pitching motion; conversely, the variation of C_l is maximized for $\phi = 3\pi/2$, that is, when the flap actuation and the pitching movement are in phase opposition. Similarly, the C_m (Figs. 12c and 12d) shows the largest variation with respect to the clean wing case for $\phi = \pi/2$ and $\phi = 3\pi/2$. When the flap displacement is in phase with the pitching motion ($\phi = \pi/2$), the nose-up pitching moment is enhanced, thus causing the largest variation of C_m for the investigated angle of attack range. Differently, for $\phi = 3\pi/2$, the nose-up pitching moment is reduced, thus causing a flatter hysteresis cycle. The amplitude of the hysteresis cycle, instead, is maximized for $\phi = 0$ and π, that is, the pitching and flap movements are in phase.

Test case B (Figs. 13a and 13b) shows a similar behavior as test case A. The minimum in-cycle variation of C_l is measured for $\phi = \pi/2$ and the maximum in-cycle variation is measured for $\phi = 3\pi/2$.

The maximum variation of C_l with the angle of attack is lower when transition is forced. Similarly to the static case, C_m (Figs. 13c and 13d) shows a peak in correspondence of the pitching movement reversal ($t/\tau \approx 0.5$). The peak intensity depends on the flap motion, especially when transition is forced. The effect of the flap is to rotate the C_m curve with respect to the fixed flap configuration, as also discussed for test case A. The maximum variation of C_m with the angle of attack is again measured for $\phi = \pi/2$ and $\phi = 3\pi/2$.

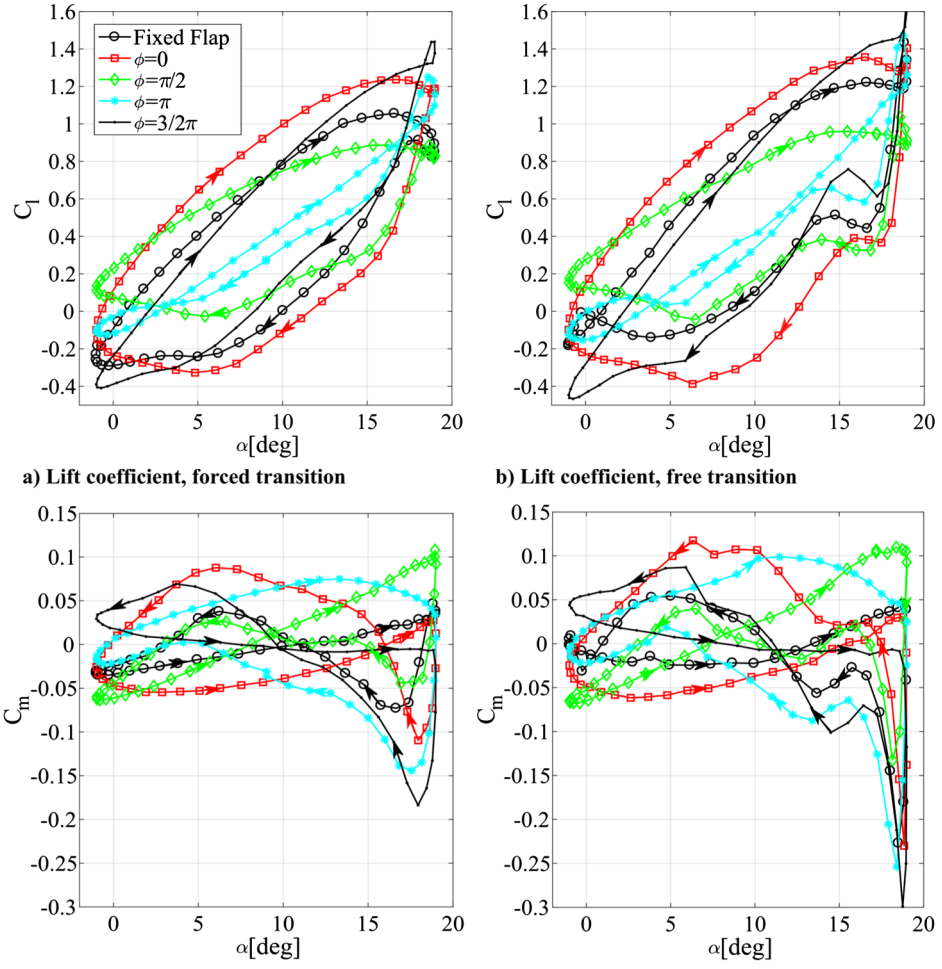

a) Lift coefficient, forced transition

b) Lift coefficient, free transition

c) Pitching moment coefficient, forced transition

d) Pitching moment coefficient, free transition

Fig. 13 Comparison of the lift and pitching moment coefficients for different flap actuation phases. Test case B: $\alpha_m = 9°$, $\alpha_{0,F} = 10°$.

Table 3 Flap control derivatives and respective coefficients of determination

	$\partial C_l/\partial\alpha_F$	$\partial C_m/\partial\alpha_F$
Forced transition	-0.027 ($R^2 = 0.96$)	-0.0049 ($R^2 = 0.96$)
Free transition	-0.023 ($R^2 = 0.84$)	-0.0052 ($R^2 = 0.81$)

As expected, the effect of the flap on the loads in dynamic cases fits with the expected behavior outlined by the static characterization: negative deflection increases the circulation, inducing higher lift on the wing and a nose-up pitching moment. Nevertheless, in agreement with Gerontakos and Lee [27], the flap is not able to create a strong modification of the flow behavior around the wing: typical features observed in the loading cycles for zero flap cases are preserved for dynamically deflecting flap cases. These two considerations may be considered as hints of linearity of the flap effect on the loads in dynamic flow conditions. In the next paragraph, the possibility of linearization of the flap effect will be investigated.

In Figs. 12 and 13, the arrow line plotted on the top of the C_l and C_m curves shows the phase direction of the load loops. The change from clockwise to counterclockwise orientation suggests that the effect of the TEF is double: it alters the aerodynamic loads and influences the aerodynamic damping coefficient (see [2]), defined over the entire cycle as $\Xi_{\text{cycle}} = -1/(\pi\alpha_0^2)\oint C_m\,\mathrm{d}\alpha$. Despite the flap could be effectively used to modify the aeroelastic behavior of the blade, this aspect is not further investigated in this paper, because the main goal is the control of the unsteady loads.

E. Linearization of the Flap Contribution

Based on the observations reported in the previous subsection, a linearization approach for the flap contribution is proposed. The load coefficients measured with the flap deflected, $C_l(\alpha,\alpha_F)$ and $C_m(\alpha,\alpha_F)$, are decomposed as the linear sum of the loads at zero flap angle configuration, $C_l(\alpha,0)$ and $C_m(\alpha,0)$, and a contribution depending on the flap angle, $\Delta C_l(\alpha_F)$ and $\Delta C_m(\alpha_F)$. As a first approximation the flap contribution is considered a linear function of α_F, according to Eqs. (4):

$$C_l(\alpha,\alpha_F) = C_l(\alpha,0) + \Delta C_l(\alpha_F) = C_l(\alpha,0) + \frac{\partial C_l}{\partial\alpha_F}\alpha_F$$
$$C_m(\alpha,\alpha_F) = C_m(\alpha,0) + \Delta C_m(\alpha_F) = C_m(\alpha,0) + \frac{\partial C_m}{\partial\alpha_F}\alpha_F \quad (4)$$

where $\partial C_l/\partial\alpha_F$ and $\partial C_m/\partial\alpha_F$ are the control derivatives of the flap.

In the following, the control derivatives are obtained by a linear fit of the steady loads. The values of the control derivatives are summarized in Table 3 along with the respective coefficients of determination R^2.

The load coefficients, in steady conditions, after removing the flap contribution are reported in Fig. 14. The flap contribution to lift and moment coefficients is expressed as $\Delta C_l = (\partial C_l/\partial\alpha_F)\alpha_F$ and $\Delta C_m = (\partial C_m/\partial\alpha_F)\alpha_F$, respectively. In the forced transition configuration, the C_l–ΔC_l and C_m–ΔC_m curves collapse on the zero flap angle case for pre-stall angles of attack, thus showing the linearity of the flap contribution. Similarly, in post-stall conditions, the C_l curves collapse within the scaling, thus showing that the linearity hypothesis is still valid. On the other side, the self-similarity of the C_m curves is less accurate. In free transition configuration the linearized model seems to be inaccurate to model the flap contribution; this is likely due to the presence of the sudden growth of the lift coefficient at $\alpha \approx 7°$, ascribed to a laminar separation bubble as in [42], resulting in a nonlinear behavior in the forces and in a flap contribution effect both dependent on α_F and α.

The linearized model of the flap contribution is applied to the dynamic test case A. The C_l–ΔC_l curves, after removing the flap contribution, are presented in Figs. 15a and 15b for forced and free transition, respectively. In both cases and for the different flap phase delays, a good collapse of the curves is obtained. For free transition configuration, the overlap between the C_l–ΔC_l curves is less accurate. This can be ascribed to the dynamic of the laminar bubble at the trailing edge, as previously discussed in Sec. III.A, that causes an unpredictable and strongly nonlinear change of the airfoil aerodynamic shape. Figures 15c and 15d show the results of the linearization of the flap contribution on C_m. For the forced transition configuration, the linearization shows a good collapse of

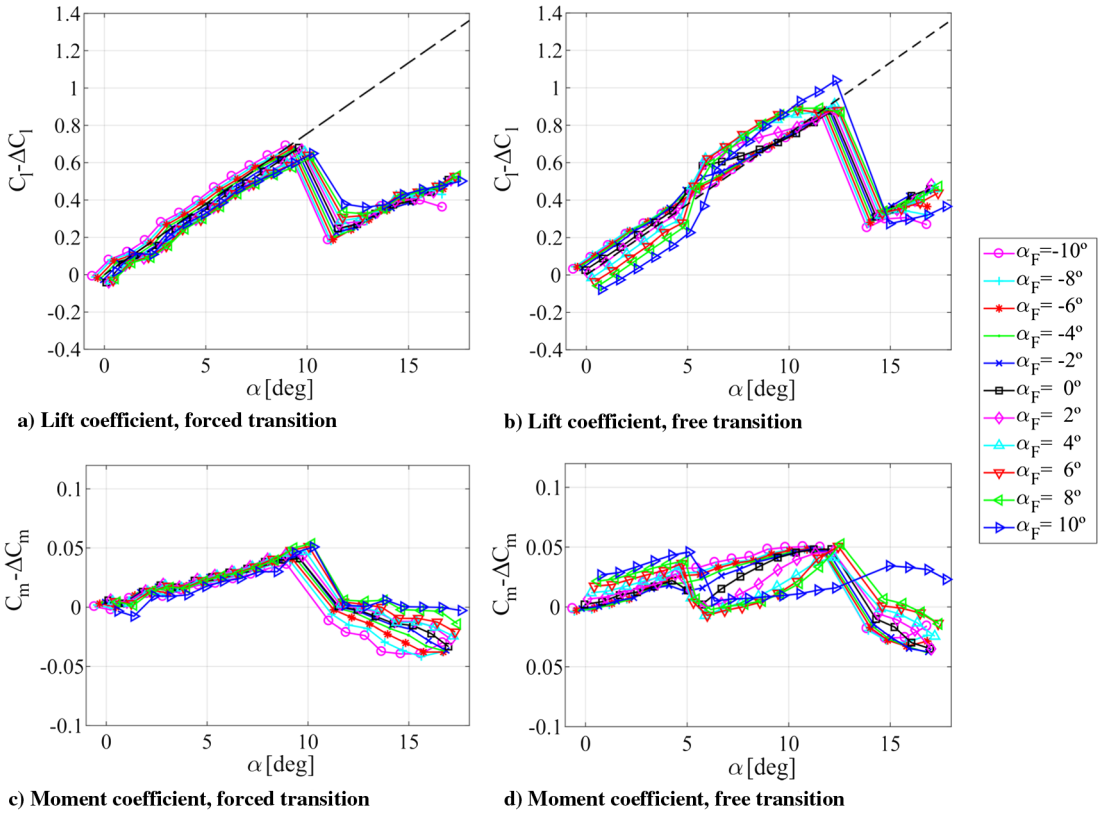

a) Lift coefficient, forced transition **b) Lift coefficient, free transition**

c) Moment coefficient, forced transition **d) Moment coefficient, free transition**

Fig. 14 Static lift and pitching moment coefficients removing the linearized flap contribution.

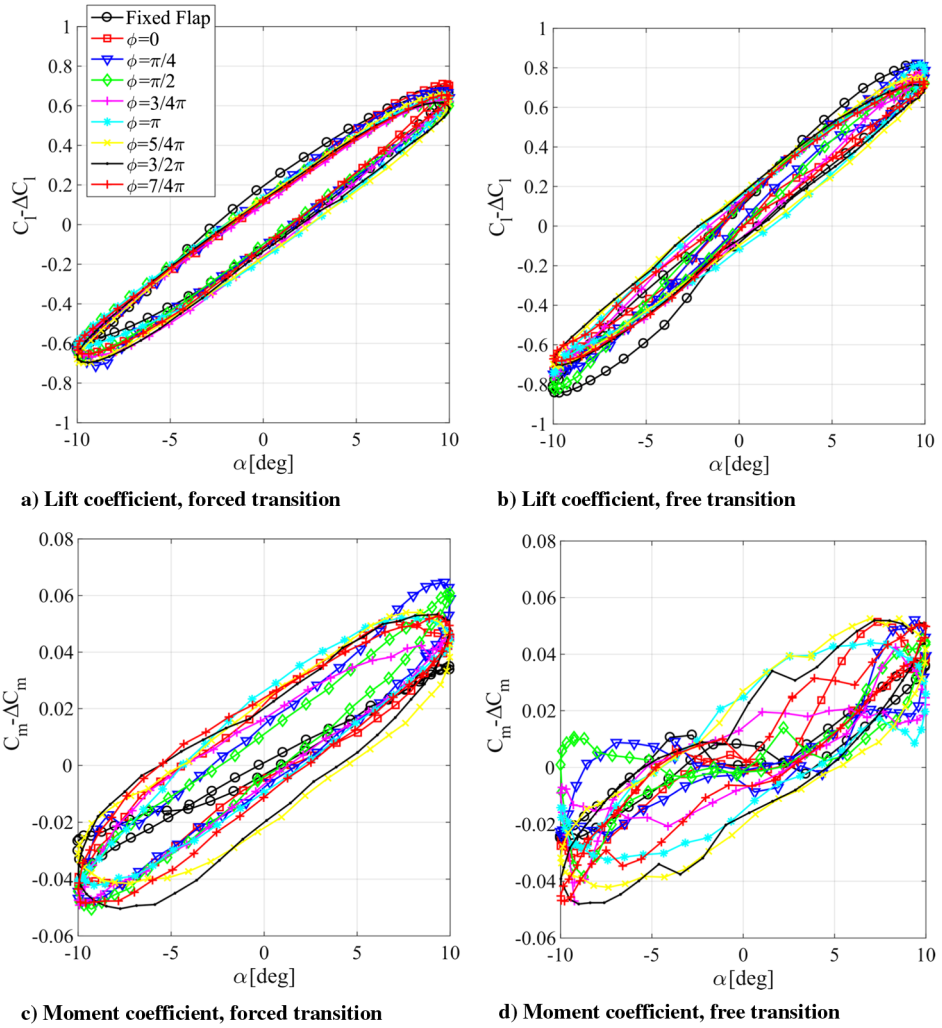

a) Lift coefficient, forced transition **b) Lift coefficient, free transition**

c) Moment coefficient, forced transition **d) Moment coefficient, free transition**

Fig. 15 Lift and pitching moment coefficients after removing the linearized flap contribution. Test case A: $\alpha_m = 0°$, $\alpha_{0,F} = 10°$.

the C_m–ΔC_m curves. For both configurations, despite all the curves almost collapse to the fixed flap curve, the cases with flap actuation present larger hysteresis amplitude with respect to the case with fixed flap.

The same operation of linearly subtracting the flap contribution is carried out for the dynamic test case B (Figs. 16a and 16b). Both for free and forced transition, all the curves tend to collapse to the fixed flap case also in deep stall conditions. For the forced transition regime, the differences between the collapsed curves, although being small, are mainly measured during the downstroke of the pitching motion (post-stall regime), whereas there is a better matching of the curves during the upstroke (attached-flow regime). Also for the airfoil with free transition the matching is satisfactory for almost the entire cycle. A noticeable difference between the curves can be observed before and after the pitch reversal. The disagreement before the pitch reversal might be associated with the nonlinear behavior in pre-stall conditions as also observed for the static case. Differently, the differences measured after the pitch reversal might be associated with the occurrence of the second lift peak whose intensity and position appear to slightly vary depending on the flap actuation. Similarly, by removing the linearized flap effect from the pitching moment, in forced transition case (Fig. 16c), a good agreement with the fixed flap case can be observed during the upstroke and during almost all the downstroke for smaller angles of attack. After the pitching stroke reversal, when the flow is separated and a large recirculation zone is present on the suction side, the flap effect seems to be strongly nonlinear. In the free transition case (Fig. 16d) although all the curves still tend to collapse toward the fixed flap case, the matching is worse than in the forced transition case.

IV. Conclusions

A strategy to control the unsteady aerodynamic forces on airfoils for wind turbine blades has been proposed and tested. To reproduce the operative conditions of a wind turbine blade, a 2D wing is operated at $Re = 1.3 \times 10^5$ in pitching and heaving motions, with reduced frequency equal to $k = 0.1$. The forces are evaluated by integrating the differential pressure between the dorsal and ventral surfaces of the airfoil measured with 24 differential pressure sensors distributed along the chord. A boundary-layer tripping is installed on the airfoil and the results of both free and forced transition are compared. Velocity measurements have been carried out with particle image velocimetry (PIV) on the suction side of the flapping airfoil reaching deep stall conditions. The comparison between flow fields and synchronized pressure measurements has provided a link between flow structures and the generation of dynamic loads. The leading edge vortex (LEV) dynamics have been identified as the dominating cause of loads variations along the cycle; sudden drop of the pressure difference between the pressure and the suction side occurs due to the LEV detachment to the airfoil. The force and moments measurements suggest that the presence of a tripping device significantly affects this process.

The effect of the tripping to control transition and separation is investigated without flap actuation through pressure measurements. The results show that, even if not entering in deep stall, the location of the local maxima of the differential pressure fluctuations experiences large oscillations over the period, whereas this effect is minimized when forcing the boundary-layer transition. In the deep stall cases, separated flow occurs after the pitching stroke reversal both in free and forced transition configurations. The separation is less abrupt in

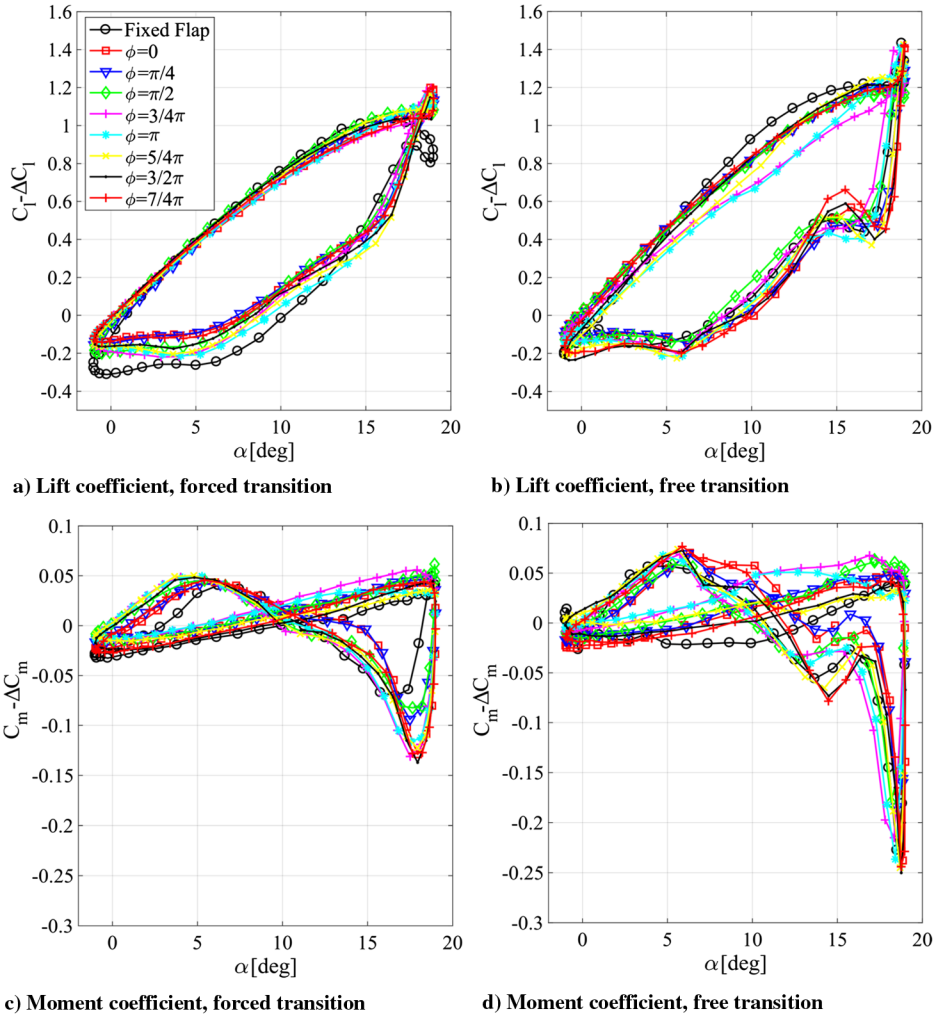

a) Lift coefficient, forced transition **b) Lift coefficient, free transition**

c) Moment coefficient, forced transition **d) Moment coefficient, free transition**

Fig. 16 Lift and pitching moment coefficients after removing the linearized flap contribution. Test case B: $\alpha_m = 9°$, $\alpha_{0,F} = 10°$.

the forced transition case, as testified by the reduced hysteresis effects. This behavior suggests a possible use of leading-edge roughness as a passive mean to reduce load variations and to back-up active control methods.

The effect of the flap on the dynamic loads has been analyzed for a set of sinusoidal flap motions with different phase shifts with respect to the pitching motion. The results confirm the capability of the flap to control the total circulation over the airfoil in dynamic conditions, regardless of the transition forcing and of the wing motion. The flap effect on forces/moments generation is weakly dependent on the dynamic stall phenomenon itself and can be linearized. In the free transition case, however, the flap effect is influenced by the instantaneous angle of attack, as confirmed also by the measurements in static conditions.

The aerodynamic loads can be modeled as the sum of the zero flap angle loads and of a contribution depending linearly on the flap deflection. The flap contribution has been modeled through the flap control derivatives measured in steady flow conditions. The applied model provides a good prediction of the loads on the airfoil with trailing edge flap. The extension to the onset of deep stall of a linear prediction for the flap effect on forces and moments has been attempted. Overall, a linearization of the flap effect appears to be perfectly suitable for attached flows on airfoils with boundary-layer tripping. The nonlinearities experienced by the cases with free transition and during the dynamic stall and the further reattachment are instead poorly approximated by a linear flap model, although they might be used as a first-order estimation.

The results suggest that aerodynamic loads can be mitigated via a linear actuation of the flap based on instantaneous load measurements. A study of the 3D problem would be the next step to assess the effectiveness of the flap on a real blade. The dynamic stall would be strongly affected by the presence of finite-wing effects (through the influence of the tip vortex), by mutual interference between different blade sections, and by the different conditions along the blade span. This results in a strong three-dimensional behavior of the dynamic stall (see, e.g., [43–45]). In this scenario, the linearization of the flap effects on the loads obtained for a fully 2D configuration might be improved for a quasi-2D case.

The experiments have been performed at a reduced frequency representative of a wind turbine motion. Helicopter rotors, instead, experience higher reduced frequencies for which nonlinear effects might be stronger. Moreover, despite the wing and the flap move with the same frequency, the motion/force lag can differ. As a matter of fact, Theodorsen [46] showed that, for a purely pitching airfoil, higher reduced frequencies ($k > 0.1$) introduce a motion/force lag, which in part depends on the effect of the added-mass forces (arising from the angular velocity and acceleration of the airfoil in the fluid). The periodic flap deflection generates a similar effect. Based on these arguments, the extension of present results to helicopter rotors is, thus, not straightforward and requires further analysis.

Acknowledgments

This research is supported by the Dutch Technology Foundation STW No. 12173. S. Discetti, A. Ianiro, and M. Raiola have been partially supported by Grant TRA2013-41103-P of the Spanish Ministry of Economy and Competitiveness. This grant includes FEDER funding.

References

[1] Barlas, T. K., and Van Kuik, G. A. M., "Review of State of the Art in Smart Rotor Control Research for Wind Turbines," *Progress in Aerospace Sciences*, Vol. 46, No. 1, 2010, pp. 1–27. doi:10.1016/j.paerosci.2009.08.002

[2] Corke, T. C., and Thomas, F. O., "Dynamic Stall in Pitching Airfoils: Aerodynamic Damping and Compressibility Effects," *Annual Review of Fluid Mechanics*, Vol. 47, No. 1, 2015, pp. 479–505. doi:10.1146/annurev-fluid-010814-013632

[3] Shipley, D. E., Miller, M. S., and Robinson, M. C., *Dynamic Stall Occurrence on a Horizontal Axis Wind Turbine Blade*, National Renewable Energy Lab., NREL/TP-442-6912; CONF-950116-8, Golden, CO, 1995, https://www.osti.gov/scitech/biblio/111926.

[4] McCroskey, W. J., "Unsteady Airfoils," *Annual Review of Fluid Mechanics*, Vol. 14, No. 1, 1982, pp. 285–311. doi:10.1146/annurev.fl.14.010182.001441

[5] Corke, T. C., Bowles, P. O., He, C., and Matlis, E. H., "Sensing and Control of Flow Separation Using Plasma Actuators," *Philosophical Transactions of the Royal Society A*, Vol. 369, No. 1940, 2011, pp. 1459–1475. doi:10.1098/rsta.2010.0356

[6] Shyy, W., Lian, Y., Tang, J., Viieru, D., and Liu, H., *Aerodynamics of Low Reynolds Number Flyers*, Cambridge Univ. Press, Cambridge, U.K., 2008, pp. 107–108.

[7] Harris, F. D., Jr., Tarzanin, F. J., Jr., and Fisher, R. K., "Rotor High Speed Performance, Theory Versus Test," *Journal of the American Helicopter Society*, Vol. 15, No. 3, 1970, pp. 35–44. doi:10.4050/JAHS.15.35

[8] Tarzanin, F. J., Jr., "Prediction of Control Loads due to Blade Stall," *Journal of the American Helicopter Society*, Vol. 17, No. 2, 1972, pp. 33–46. doi:10.4050/JAHS.17.33

[9] Young, W. H., Jr., "Fluid Mechanics Mechanisms in the Stall Process for Helicopters," Natl. Aeronaut. Space Admin., Tech. Rept. NASA-TM-81956, Washington, D.C., 1981.

[10] Hansen, A. C., and Butterfield, C. P., "Aerodynamics of Horizontal-Axis Wind Turbines," *Annual Review of Fluid Mechanics*, Vol. 25, No. 1, 1993, pp. 115–149. doi:10.1146/annurev.fl.25.010193.000555

[11] Ol, M. V., Bernal, L., Kang, C. K., and Shyy, W., "Shallow and Deep Dynamic Stall for Flapping Low Reynolds Number Airfoils," *Experiments in Fluids*, Vol. 46, No. 5, 2009, pp. 883–901. doi:10.1007/s00348-009-0660-3

[12] Baik, Y. S., Bernal, L. P., Granlund, K., and Ol, M. V., "Unsteady Force Generation and Vortex Dynamics of Pitching and Plunging Aerofoils," *Journal of Fluid Mechanics*, Vol. 709, Oct. 2012, pp. 37–68. doi:10.1017/jfm.2012.318

[13] Pitt Ford, C. W., and Babinsky, H., "Lift and the Leading-Edge Vortex," *Journal of Fluid Mechanics*, Vol. 720, April 2013, pp. 280–313. doi:10.1017/jfm.2013.28

[14] Prangemeier, T., Rival, D., and Tropea, C., "The Manipulation of Trailing-Edge Vortices for an Airfoil in Plunging Motion," *Journal of Fluids and Structures*, Vol. 26, No. 2, 2010, pp. 193–204. doi:10.1016/j.jfluidstructs.2009.10.003

[15] Greenblatt, D., and Wygnanski, I., "Dynamic Stall Control by Periodic Excitation, Part 1: NACA 0015 Parametric Study," *Journal of Aircraft*, Vol. 38, No. 3, 2001, pp. 430–438. doi:10.2514/2.2810

[16] Sun, M., and Sheikh, S., "Dynamic Stall Suppression on an Oscillating Airfoil by Steady and Unsteady Blowing," *Aerospace Science and Technology*, Vol. 3, No. 6, 1999, pp. 355–366. doi:10.1016/S1270-9638(00)86426-3

[17] Weaver, D., McAlister, K. W., and Tso, J., "Control of VR7 Dynamic Stall by Strong Steady Blowing," *Journal of Aircraft*, Vol. 41, No. 6, 2004, pp. 1404–1413. doi:10.2514/1.4413

[18] Lombardi, A. J., Bowles, P. O., and Corke, T. C., "Closed-Loop Dynamic Stall Control Using a Plasma Actuator," *AIAA Journal*, Vol. 51, No. 5, 2013, pp. 1130–1141. doi:10.2514/1.J051988

[19] Post, M. L., and Corke, T. C., "Separation Control Using Plasma Actuators: Dynamic Stall Vortex Control on Oscillating Airfoil," *AIAA Journal*, Vol. 44, No. 12, 2006, pp. 3125–3135. doi:10.2514/1.22716

[20] Heine, B., Mulleneres, K., Joubert, G., and Raffel, M., "Dynamic Stall Control by Passive Disturbance Generators," *AIAA Journal*, Vol. 51, No. 9, 2013, pp. 2086–2097. doi:10.2514/1.J051525

[21] Martin, P. B., Wilson, J. S., Berry, J. D., Wong, T.-C., Moultron, M., and McVeigh, M. A., "Passive Control of Compressible Dynamic Stall," *26th AIAA Applied Aerodynamics Conference*, AIAA Paper 2008-7506, 2008. doi:10.2514/6.2008-7506

[22] Traub, L. W., Miller, A., and Rediniotis, O., "Effects of Active and Passive Flow Control on Dynamic-Stall Vortex Formation," *Journal of Aircraft*, Vol. 41, No. 2, 2004, pp. 405–408. doi:10.2514/1.2591

[23] Ekaterinaris, J. A., "Numerical Investigations of Dynamic Stall Active Control for Incompressible and Compressible Flows," *Journal of Aircraft*, Vol. 39, No. 1, 2002, pp. 71–78. doi:10.2514/2.2897

[24] Florea, R., and Wake, B. E., "Parametric Analysis of Directed-Synthetic Jets for Improved Dynamic-Stall Performance," *41st AIAA Aerospace Sciences Meetings*, AIAA Paper 2003-0216, 2003. doi:10.2514/6.2003-216

[25] Traub, L. W., Miller, A., and Rediniotis, O., "Effects of Active and Passive Flow Control on Dynamic-Stall Vortex Formation," *Journal of Aircraft*, Vol. 41, No. 2, 2004, pp. 405–408. doi:10.2514/1.2591

[26] Feszty, D., Gillies, E. A., and Vezza, M., "Alleviation of Airfoil Dynamic Stall Moments via Trailing-Edge-Flap Flow Control," *AIAA Journal*, Vol. 42, No. 1, 2004, pp. 17–25. doi:10.2514/1.853

[27] Gerontakos, P., and Lee, T., "Dynamic Stall Flow Control via a Trailing-Edge Flap," *AIAA Journal*, Vol. 44, No. 11, 2006, pp. 2746–2754. doi:10.2514/1.19776

[28] Gerontakos, P., and Lee, T., "Trailing-Edge Flap Control of Dynamic Pitching Moment," *AIAA Journal*, Vol. 45, No. 7, 2007, pp. 1688–1694. doi:10.2514/1.27577

[29] Gerontakos, P., and Lee, T., "PIV Study of Flow Around Unsteady Airfoil with Dynamic Trailing-Edge Flap Deflection," *Experiments in Fluids*, Vol. 45, No. 6, 2008, pp. 955–972. doi:10.1007/s00348-008-0514-4

[30] Lee, T., and Su, Y. Y., "Unsteady Airfoil with a Harmonically Deflected Trailing-Edge Flap," *Journal of Fluids and Structures*, Vol. 27, No. 8, 2011, pp. 1411–1424. doi:10.1016/j.jfluidstructs.2011.06.008

[31] Barlas, T., and Lackner, M., "Smart Rotor Blade Technology Applied to the Upwind Reference Turbine," *Proceedings of the IEA Topical Expert Meeting on the Application of Smart Structures for Large Wind Turbine Rotor Blades*, Sandia National Labs, Alberquerque, New Mexico, 2008, http://lr.home.tudelft.nl/fileadmin/Faculteit/LR/Organisatie/Afdelingen_en_Leerstoelen/Afdeling_AEWE/Wind_Energy/Research/Publications/Publications_2008/doc/Pages_from_56_Proceedings_Smart_Struct_PRELIMINARY_Small.pdf.

[32] Castaignet, D., Barlas, T., Buhl, T., Poulsen, N. K., Wedel-Heinen, J. J., Olesen, N. A., Bak, C., and Kim, T., "Full-Scale Test of Trailing Edge Flaps on a Vestas V27 Wind Turbine: Active Load Reduction and System Identification," *Wind Energy*, Vol. 17, No. 4, 2014, pp. 549–564. doi:10.1002/we.v17.4

[33] Straub, F., Anand, V., Birchette, T., and Lau, B., "SMART Rotor Development and Wind-Tunnel Test," German Society for Aeronautics and Astronautics—Lilienthal-Oberth e.V. (DGLR), Hamburg, Germany, Sept. 2009, Paper 1200, https://ntrs.nasa.gov/search.jsp?R=20090035867.

[34] Kottapalli, S., "Enhanced Correlation of SMART Active Flap Rotor Loads," *52nd AIAA/ASME/ASCE/AHS/ASC Structures, Structural Dynamics and Materials Conference*, AIAA Paper 2011-1874, April 2011. doi:10.2514/6.2011-1874

[35] Abbott, I. H., and Von Doenhoff, A. E., *Theory of Wing Sections, Including a Summary of Airfoil Data*, Dover Publ., New York, 1959.

[36] Lignarolo, L. E. M., Ragni, D., Krishnaswami, C., Chen, Q., Ferreira, C. S., and Van Bussel, G. J. W., "Experimental Analysis of the Wake of a Horizontal-Axis Wind-Turbine Model," *Renewable Energy*, Vol. 70, Oct. 2014, pp. 31–46. doi:10.1016/j.renene.2014.01.020

[37] Moffat, R. J., "Describing the Uncertainties in Experimental Results," *Experimental Thermal and Fluid Science*, Vol. 1, No. 1, 1988, pp. 3–17. doi:10.1016/0894-1777(88)90043-X

[38] Fuglsang, P., Antoniou, I., Sørensen, N. N., and Aagaard Madsen, H., "Validation of a Wind Tunnel Testing Facility for Blade Surface Pressure Measurements," Risø National Lab., Risø-R-981(EN), Denmark, 1998.

[39] Mendez, M. A., Raiola, M., Masullo, A., Discetti, S., Ianiro, A., Theunissen, R., and Buchlin, J. M., "POD-Based Background Removal for Particle Image Velocimetry," *Experimental Thermal and Fluid Science*, Vol. 80, Jan. 2017, pp. 181–192. doi:10.1016/j.expthermflusci.2016.08.021

[40] Westerweel, J., "Fundamentals of Digital Particle Image Velocimetry," *Measurement Science and Technology*, Vol. 8, No. 12, 1997, pp. 1379–1392. doi:10.1088/0957-0233/8/12/002

[41] Deperrois, A., "XFLR5 Analysis of Foils and Wings Operating at Low Reynolds Numbers," Feb. 2013, http://www.xflr5.com [retrieved 14 Feb. 2017].

[42] Timmer, W. A., "Two-Dimensional Low-Reynolds Number Wind Tunnel Results for Airfoil NACA 0018," *Wind Engineering*, Vol. 32, No. 6, 2008, pp. 525–537. doi:10.1260/030952408787548848

[43] Spentzos, A., Barakos, G. N., Badcock, K. J., Richards, B. E., Coton, F. N., and Galbraith, R. A. M. D., "Computational Fluid Dynamics Study of Three-Dimensional Dynamic Stall of Various Planform Shapes," *Journal of Aircraft*, Vol. 44, No. 4, 2007, pp. 1118–1128. doi:10.2514/1.24331

[44] Jain, R., Le Pape, A., Costes, M., Richez, F., and Smith, M., "High-Resolution CFD Predictions for Static and Dynamic Stall of a Finite-Span OA209 Wing," *Proceedings of the 72nd Annual Forum of the American Helicopter Society*, American Helicopter Soc. (AHS) Paper 0830-0900, May 2016, https://vtol.org/store/product/highresolution-cfd-predictions-for-static-and-dynamic-stall-of-a-finitespan-oa209-wing-11371.cfm.

[45] Kaufmann, K., Merz, C. B., and Gardner, A. D., "Dynamic Stall Simulations on a Pitching Finite Wing," *Journal of Aircraft*, Vol. 54, No. 4, 2017, pp. 1303–1316. doi:10.2514/1.C034020

[46] Theodorsen, T., "General Theory of Aerodynamic Instability and the Mechanism of Flutter," NACA Report 496, Washington, D.C., 1935.

F. N. Coton
Associate Editor